

Effects of Sintering Behaviors on Dimensional Accuracy, Surface Quality, and Mechanical Properties of Stereolithography-printed 3Y-ZrO₂ Ceramics

Cheng Zhang

Shandong University

Zhaoliang Jiang (✉ jiangzhaoliang@sdu.edu.cn)

Shandong University <https://orcid.org/0000-0002-6258-7869>

Li Zhao

Shandong University

Weiwei Guo

Shandong University

Chengpeng Zhang

Shandong University

Research Article

Keywords: Sintering behavior, Dimensional accuracy, Surface quality, Mechanical property, Stereolithography

Posted Date: June 16th, 2021

DOI: <https://doi.org/10.21203/rs.3.rs-618580/v1>

License:   This work is licensed under a Creative Commons Attribution 4.0 International License.

[Read Full License](#)

Effects of sintering behaviors on dimensional accuracy, surface quality, and mechanical properties of stereolithography-printed 3Y-ZrO₂ ceramics

Cheng Zhang¹, Zhaoliang Jiang^{1*}, Li Zhao¹, Weiwei Guo¹, Chengpeng Zhang¹

1. Key Laboratory of High Efficiency and Clean Mechanical Manufacture (Ministry of Education), National Demonstration Center for Experimental Mechanical Engineering Education, School of Mechanical Engineering, Shandong University, Jinan, 250061, PR China

*Corresponding author: Zhaoliang Jiang.

E-mail: jiangzhaoliang@sdu.edu.cn.

Abstract

Sintering process is essential to acquire the final components by stereolithography (SLA), which is a promising additive manufacturing technology for the fabrication of complex, custom-designed dental implants. 3Y-ZrO₂ ceramics at different sintering behaviors in air atmosphere were successfully obtained in this study. Firstly, the curing properties of homemade pastes were studied, and the penetration depth and critical exposure of the pastes were calculated as 17.2 μm and 4.80 mJ/cm², respectively. The green ceramic parts were performed at 154 mW laser power and 6000 mm/s scanning speed. Then, the dimensional accuracy, surface quality, and mechanical properties of 3Y-ZrO₂ ceramics were investigated. The shrinkages of length, width, and height were 26%~27 %, 30%~31 %, and 27%~33 % in sintered ceramics, respectively. The Ra values of XOY, YOZ, and XOZ surfaces showed an anisotropic feature, and they were smallest as 0.52 μm, 2.40 μm, and 2.46 μm, respectively. Meanwhile, the mechanical properties presented a similar trend that they grew first and then dropped at various sintering behaviors. The optimal parameters were 1500 °C, 60 min, and 4 °C/min, and the maximum relative density of 96.18 %, Vickers hardness of 12.45 GPa, and fracture toughness of 6.35 MPa·m^{1/2} were achieved. Finally, the X-ray diffraction (XRD) and energy-dispersive spectroscopy (EDS) analysis demonstrated that no change was

observed in crystal transformation and phase composition, and the organic was completely removed in sintered ceramics. This research is expected to provide a technical guide for the fabrication of ceramics for dental implants using SLA technique.

Keywords

Sintering behavior; Dimensional accuracy; Surface quality; Mechanical property; Stereolithography

1. Introduction

Zirconia (ZrO_2) ceramics are considered as good potentiality for dental restorations and hip replacements owing to their high fracture strength, excellent wear resistance, and biocompatibility [1,2]. As a dental implant material, these properties of ZrO_2 ceramics make it hard to fabricate with complex shapes. Traditional methods such as hot-press and spark plasma sintering have been adopted to manufacture ZrO_2 ceramics for biological applications [3,4]. Rapid developments in computer-aided design and computer-aided manufacturing (CAD/CAM) technique have facilitated the fabrication of ZrO_2 oral restorations by machining [5,6], and milled ZrO_2 ceramics have shown satisfactory osseointegration and good tissue biocompatibility after a sufficient healing period [7]. However, these forming technologies need to use molds or cutting tools, which lead to the waste of raw materials and extend the production cycles. Meanwhile, the machining process would produce microcracks and defects on the surface. Thus, a method for direct fabrication of custom-designed teeth without the demand for mechanical machining would provide a huge improvement in dental implants.

Compared with traditional machining methods, additive manufacturing has recently provided a new resolution for these problems [8,9]. As reported, the 3D printing technologies applicable to ZrO_2 ceramics mainly include stereolithography (SLA) [10], direct ink writing (DIW) [11], digital light processing (DLP) [12], fused deposition molding (FDM) [13], and selective laser sintering/melting (SLS/SLM) [14,15]. The SLA technology provides not only a smoother surface finish, but also an improved precision feature in production, which is suitable for fabricating custom-designed dental implants.

Sintering process is an essential solution to acquire excellent properties after the green bodies are formed, which have an obvious influence on the final parts fabricated by SLA [16,17]. Li et al. investigated the effects of sintering temperature on microstructure and mechanical properties of Al₂O₃ ceramics, and the flexural strength of 26.7 MPa, Vickers hardness of 198.5 HV, nanoindentation hardness of 33.1 GPa, bulk density of 2.5 g/cm³, and open porosity of 33.8% at 1350 °C in argon atmosphere [18]. Xing et al. measured the flexural strength, fracture toughness, hardness, and density values of ZrO₂ ceramics as 1154 ± 182 MPa, 6.37 ± 0.25 MPa·m^{1/2}, 13.90 ± 0.62 GPa, and 99.3 %, respectively [19]. Meanwhile, Wu et al. proposed an integrated approach to manufacture 3D-printed alumina toughened zirconia (ATZ) samples and showed the lowest aging rate and phase transformation depth at 1550 °C [20]. Zheng et al. investigated the surface morphologies and mechanical properties of zirconia toughened alumina (ZTA) composites, and the final 3D-printed parts exhibited high relative density and good interlayer combinations at 1600 °C [21]. Liu et al. studied on the mechanical properties of the printed ZTA composites sintered at different sintering temperatures and holding time. They found the actual density, hardness, and fracture toughness of the samples were 3.75 g/cm³, 14.1 GPa, and 4.05 MPa·m^{1/2} at 1500 °C and 60 min, respectively [22]. These investigations focused on the mechanical properties of composite ceramics at different sintering temperatures alone. However, the sintering behaviors including sintering temperature, hold time, and sintering rate could not be studied systematically. Meanwhile, the surface quality and precision of the 3D-printed samples would not be taken into account.

In this study, the curing properties of homemade 3Y-ZrO₂ pastes were firstly discussed in terms of cure depth and cure width, which would offer a suitable laser power and scanning speed for the fabrication of the green ceramic parts. Then, the green ceramic parts were heated to remove the organic from the green ceramic bodies and prepare for subsequent sintering. Based on the thermal analysis, the effects of sintering temperature (1400 °C, 1450 °C, 1500 °C, 1550 °C), holding time (0 min, 30 min, 60 min, 90 min), and sintering rate (2 °C/min, 4 °C/min, 6 °C/min, 8 °C/min) on the dimensional accuracy, surface quality, and mechanical properties of 3Y-ZrO₂ ceramics

were analyzed. Finally, the crystal transformation and phase composition were identified by the X-ray diffraction (XRD) and energy-dispersive spectroscopy (EDS). The results of this study can reveal the optimal sintering behaviors for manufacturing 3Y-ZrO₂ ceramic parts and provide an important reference for dental implants.

2. Material and methods

2.1 Materials

Commercially available 3Y-ZrO₂ powders (Shanghai Yaoyi Alloy Material Co., Ltd., China) with 99.9% purity and a particle size of 0.5 μm were applied in this study. A silane coupling agent (KH560, 1.069 g/cm³ density, 1.427 refractive index, A-187, Union Carbide Corp, USA) was selected to improve the compatibility of ceramic powders and organic resins in pastes. A ditrimethylolpropane tetraacrylate (Di-TMPTA, 1.096 g/cm³ density, 99% purity, Guangzhou, China) was used as the matrix resins of the ceramic pastes, and a poly [oxy(methyl-1,2-ethanediyl)] (NPG2PODA, 1.10 g/cm³ density, 1.467 refractive index, DSM-AGI, Netherlands) was applied to reduce the viscosity of Di-TMPTA-based premixed resins. A 1-hydroxycyclohexyl phenyl ketone photo initiator (Irgacure 184, 1.17 g/cm³ density, RYOJI, Germany) was used for UV light curing in SLA process. Finally, 75 wt.% 3Y-ZrO₂ ceramic suspensions were prepared successfully and the detailed manufacturing processes were presented in our previous study [23].

2.2 Fabrication process

To take the shrinkage into consideration, the original dimensions were set by the CAD file to be of 30 mm×4 mm×3 mm (Length×Width×Height). Subsequently, the data were imported into the SLA machine (Ceramaker 300 system, 3D CERAM, France). 3Y-ZrO₂ ceramic suspensions were uniformly paved on the working platform by a scraper, and an ultraviolet laser (355 nm in wavelength, 40 μm in spot diameter) was scanned the suspensions to create horizontal planes in a layer-by-layer fashion. A standard alternating x/y raster scanning mode was adopted in each layer for the reason that the pattern could reduce stress concentration compared with a unique x or y scanning mode [19]. Then, the platform moved down to submerge the solidified layer

by new suspensions after forming a layer. These steps were repeated until the entire green parts were eventually obtained.

Sintering process was an extremely easy defect stage in forming the ceramic parts, and the unsuitability of the process caused some cracks and warpages of the ceramics [24,25]. Thus, selecting suitable sintering behavior was an essential approach to control the forming performances of the final ceramic parts. Before this, the thermal treatments were taken to exhaust the photosensitive resins after printing. Thermogravimetric analysis (TGA) and differential scanning calorimetry (DSC) were recorded with a TGA/DSC-QMS analyzer (TGA/DSC1/1100LF, Mettler Toledo, Switzerland) to investigate the pyrolysis of photosensitive resins in debinding process aiming at judging whether the toxic substances could be completely eliminated. In this evaluation, 24.1422 mg of the printed 3Y-ZrO₂ ceramic samples were heated from room temperature to 1000 °C with a heating rate of 5 °C/min in air atmosphere. The experimental results were analyzed using a TA Analyzer software. The stages of weight loss, the onset temperature of thermal decomposition, the maximum thermal decomposition temperature, and the final thermal decomposition temperature of the organic can be determined from the TG-DSC curves [26]. The green bodies underwent debinding and sintering in a muffle furnace (KSL-1700X-A3, Hefei Ke Jing Materials Technology Co., Ltd, China). Firstly, the green parts were heated to 600 °C with a heating rate of 0.2 °C/min and held for 10 h, then heated to 1000 °C with a heating rate of 1 °C/min and held for 3 h to burnout the binder in air atmosphere. Then, the samples were heated with different target sintering temperatures (1400 °C, 1450 °C, 1500 °C, 1550 °C), and target holding time (0 min, 30 min, 60 min, 90 min), and target sintering rates (2 °C/min, 4 °C/min, 6 °C/min, 8 °C/min). Finally, the samples were cooled to 500 °C with a heating rate of 5 °C/min and subsequently subjected to furnace cooling to obtain the final ceramic components.

2.3 Characterization

The cure depth and cure width of the green bodies were measured using a digital micrometer thickness gauge with a range of 0~10 mm and accuracy of 0.001 mm (547-

400, Mitutoyo, Japan) and a 3D laser microscope (VK-X200K, KEYENCE, Japan), respectively. The surface roughness of three directions (Length \times Width \times Height) were also measured by a 3D laser microscope. The density of the sintered samples was measured by the Archimedes method using distilled water, and the relative density was calculated by the ratio of the actual density to the theoretical density (the theoretical density of zirconia ceramic is 6.10 g/cm³). The edges and surfaces of all samples were chamfered and polished to reduce the stress concentration. In the hardness experiment, the diamond Vickers indenter was indented five times at each sample with 196 N and 15 s dwell time (HVS-50, Airit, China).

The Vickers hardness H_v (MPa) of the sintered 3Y-ZrO₂ ceramics was calculated in Equation (1):

$$H_v = \frac{1.8544P}{(2a)^2}$$

(1)

Where P was applied load (196N was adopted in this study), $2a$ was diagonal length of Vickers indenters observed by the 3D laser microscope (mm).

The fracture toughness K_{IC} (MPa \cdot m^{1/2}) of the sintered ceramics was calculated based on the hardness test, which was satisfied in Equation (2):

$$K_{IC} = 0.203 \times (c/a)^{-3/2} \times \sqrt{a} \times H_v$$

(2)

Where c was the half of crack length (mm), a was the half of diagonal length of Vickers indenters (mm), and H_v was the Vickers hardness (MPa).

The fracture surfaces of the sintered 3Y-ZrO₂ ceramics were coated with a thin layer of gold for 120 s to achieve higher resolution, and the morphologies and microstructure were observed and analyzed by a scanning electron microscopy (SEM, ZEISS, OXFORD Instruments) and energy-dispersive spectroscopy (EDS, PV9900, Philips, Netherlands). The possible crystal transformations and phase compositions of the 3Y-ZrO₂ ceramic powders, printed, debinded, and sintered samples were characterized by the X-ray diffraction (XRD, Hitachi, PAX-10A-X, Japan). The XRD analysis were conducted in a 2θ range between 10 ° and 80 ° with a scanning speed of 10 °/min using

Cu K α radiation.

3. Results and discussion

3.1 Dimensional accuracy

Cure depth (C_d) and cure width (C_w) were important parameters which determine the accuracy and speed in SLA process. Thus, the curing properties of homemade pastes were investigated before the fabrication of the green 3Y-ZrO₂ ceramic parts. In an ideal state, the absorption of laser light by liquid photosensitive resins generally confirmed to the Beer-Lambert, which was presented in Equation (3) [27]. Exposure energy E was related to laser power P , scanning speed v , and laser spot diameter w_0 in SLA process [28,29], and these parameters were satisfied in Equation (4).

$$C_d = D_p \ln(E/E_c) = D_p (\ln E - \ln E_c) = D_p \ln E - D_p \ln E_c, \quad (3)$$

$$E = \frac{\sqrt{2}P}{\sqrt{\pi}w_0v}. \quad (4)$$

Where C_d was cure depth; D_p was penetration depth, E was exposure energy; E_c was critical exposure; P was laser power; v was scanning speed, and w_0 was laser spot diameter.

The honeycomb structure was reduced in size until the internal grid structure was composed of only a single scanning line in this study. Fig. 1 shows the cure depth and cure width of the 3Y-ZrO₂ suspensions at different laser powers and scanning speeds. In Fig. 1 (a), when the laser power increased from 117 mW to 133 mW, 154 mW, 182 mW, and 208 mW with the same scanning speed of 6000 mm/s, the $\ln E$ values ranged from 3.66 mJ/cm² to 3.79 mJ/cm², 3.94 mJ/cm², 4.10 mJ/cm², and 4.24 mJ/cm², respectively. The C_d mean values were measured as 35.98 μ m, 38.20 μ m, 40.80 μ m, 43.55 μ m, and 45.95 μ m, respectively. Meanwhile, a higher laser power represented a wider cure width. The C_w mean values were examined as 81.80 μ m, 84.30 μ m, 87.10 μ m, 90.00 μ m, and 91.46 μ m, respectively. The relationship between exposure energy and cure width is not a linear growth. In Fig. 1 (b), when the scanning speed increased from 2000 mm/s to 3000 mm/s, 4000 mm/s, 5000 mm/s, and 6000 mm/s with the same laser power of 154 mW, the $\ln E$ values decreased from 5.03 mJ/cm² to 4.63 mJ/cm²,

4.34 mJ/cm², 4.12 mJ/cm², and 3.94 mJ/cm², respectively. The C_d mean values were measured as 59.55 μm, 52.65 μm, 47.65 μm, 43.90 μm, and 40.80 μm, respectively. Different from the exposure energy, a lower scanning speed indicated a wider cure width. The C_w mean values were tested as 105.25 μm, 98.98 μm, 94.17 μm, 90.36 μm, and 87.10 μm, respectively. The linear fit of the C_d and the $\ln E$ was presented in Fig. 1 (c). Based on Equation (3), the D_p and E_c values of the 3Y-ZrO₂ suspensions were calculated as 17.2 μm and 4.80 mJ/cm², respectively.

Inset Fig. 1 Here.

Depended on the curing properties of homemade pastes, the green ceramic parts were performed at 154 mW laser power and 6000 mm/s scanning speed. Fig. 2 presents the weight loss (TG), associated derivative thermogram (DTG), and the rate of heat flow (DSC) of SLA-printed green bodies. The thermal analysis of the sample was divided into three stages in the process. The first stage (I period) was associated to the removal of physically adsorbed water from room temperature to 310 °C, with 1.56% weight loss. The second stage (II period) was involved with the thermal decomposition of the organic with the continuous heat between 310 °C and 620 °C, and the weight loss was 23.27%. In combination with the DTG and DSC curves, the greatest weight loss happened at 375 °C and 430 °C, and the endothermic peak took place at 428 °C and 621 °C in this stage. When the temperature continued to rise, the TG curve almost remained unchanged, and the weight loss was 0.27% in the third stage (III period). This indicated that the organic was almost eliminated [30,31]. According to the above-mentioned analysis, the sintering process was designed.

Inset Fig. 2 Here.

For proper fabrication of 3Y-ZrO₂ ceramics by SLA, the anisotropy of shrinkage that occurred were also studied in the sintering process [32]. Fig. 3 presents the length, width, and height of the sintered 3Y-ZrO₂ ceramics at different sintering behaviors. Different from the design values of the CAD files, the length, width, and height values of printed 3Y-ZrO₂ ceramics were 28.74 ± 0.08 mm, 3.88 ± 0.01 mm, and 2.92 ± 0.02 mm,

respectively. In Fig. 3 (a), the length, width, and height values almost kept constant with different sintering temperatures with the same holding time of 30 min and sintering rate of 0.2 °C/min. The dimension values of the sintered ceramics were largest as 21.25 ± 0.02 mm, 2.71 ± 0.02 mm, and 2.03 ± 0.08 mm at 1500 °C, respectively. In accordance, the shrinkage ratios (sintered dimension values/ printed dimension values) were also constant as 26 %, 30 %, and 31 %, respectively. Fig. 3 (b,c) show the dimension values of the sintered 3Y-ZrO₂ ceramics at different holding time with the same sintering temperature of 1500 °C and sintering rate of 0.2 °C/min, at different sintering rates with the same sintering temperature of 1500 °C and holding time of 30 min, respectively. Similarly, the sintered dimension values nearly kept unchanged with different holding time and sintering rates. In detail, the largest height value was 2.15 ± 0.03 mm at 60 min with a sintering temperature of 1500 °C and sintering rate of 0.2 °C/min, and the smallest height value was 1.95 ± 0.11 mm at 4 °C/min with a sintering temperature of 1500 °C and holding time of 30 min. In summary, the shrinkage ratios were 26%~27 %, 30%~31 %, and 27%~33 % in the length, width, and height direction at all different sintering behaviors, respectively. These constant ratios of three directions indirectly indicated that the organic was rarely remained in sintered 3Y-ZrO₂ ceramics.

Inset Fig. 3 Here.

3.2 Surface quality

To form ceramic structures by SLA successfully, the distance between two adjacent scanning lines H_s was smaller than the C_w . Meanwhile, the effective thickness of the cured layer T was less than the C_d because of the arc-sharped cross section of the curing line. Xing et al. optimized the scanning space H_s and moving distance T , and proposed that they should satisfy the relationships $H_s=1/2C_w$ and $T=3/5C_d$, respectively [33]. As a result, the H_s and T values were set as 50 μm and 25 μm in this study, respectively. Fig. 4 (a) shows a scanning path and layer-and-layer manufacturing character of SLA process effect on the surface quality. As presented in Fig. 4 (b-d), the surfaces of the SLA-printed 3Y-ZrO₂ ceramic bodies presented a clearly anisotropic feature, and the

surface roughness of XOY, YOZ, and XOZ surfaces were $R_a=0.51\ \mu\text{m}$, $R_a=1.79\ \mu\text{m}$, and $R_a=2.10\ \mu\text{m}$, respectively. The low surface roughness values proved that the quality fabricated by SLA showed a better potential than that of other 3D printing technologies [34,35]. Meanwhile, there was an obvious layer-and-layer process in the YOZ and XOZ surfaces, which demonstrated that the surface roughness on the YOZ and XOZ were quite severe than the XOY surface.

Inset Fig. 4 Here.

Fig. 5 shows the surface roughness of XOY, YOZ, and XOZ surfaces of the sintered 3Y-ZrO₂ ceramics at different sintering temperatures, holding time, and sintering rates. When the green bodies were sintered, the organic was burned out from those surfaces, which led to an increase of R_a value compared with that of the green bodies. In accordance, the R_a values of YOZ and XOZ surfaces were larger than that of XOY surface under the same conditions. Fig. 5 (a) shows the surface roughness of XOY, YOZ, and XOZ surfaces of the sintered 3Y-ZrO₂ ceramics at different sintering temperatures with the same holding time of 30 min and sintering rate of 0.2 °C/min. The R_a values of XOY, YOZ, and XOZ surfaces were smallest as 0.52 μm , 2.40 μm , and 2.46 μm at 1500 °C, respectively. Due to the absence of warpage, the R_a value of XOZ surface was a judging indicator to evaluate the surface quality and precision at different sintering conditions. The largest R_a value of XOZ surface occurred at 1550 °C as 3.44 μm resulted from the peeling or folds on the surface with a high sintering temperature. In Fig. 5 (b), the surface roughness of XOY, YOZ, and XOZ surfaces of the sintered 3Y-ZrO₂ ceramics were presented at different holding time with the same sintering temperature of 1500 °C and sintering rate of 0.2 °C/min. Similarly, the R_a values of XOY, YOZ, and XOZ surfaces were smallest as 0.52 μm , 2.40 μm , and 2.46 μm at 30 min, respectively. However, when the holding time exceeded 30 min, the surface roughness of XOZ surface was more severe, and the R_a values were 3.18 μm and 3.33 μm at 60 min and 90 min, respectively. Fig. 5 (c) displays the surface roughness of XOY, YOZ, and XOZ surfaces of the sintered 3Y-ZrO₂ ceramics at different sintering rates with the same sintering temperature of 1500 °C and holding time of 30 min. The R_a

values of XOY, YOZ, and XOZ surfaces were smallest as 0.52 μm , 2.40 μm , and 2.46 μm at 2 $^{\circ}\text{C}/\text{min}$, respectively. In summary, the sintering temperature and holding time played dominated roles in surface roughness, especially the Ra value of XOZ surface. In contrast, the sintering rate played a little effect indicated by the Ra values. This indicated that increasing sintering rate was a reliable solution to reduce manufacturing time under the fundamental premise of surface quality.

Inset Fig. 5 Here.

3.3 Mechanical properties and microstructure

Fig. 6 presents the mechanical properties of the sintered 3Y-ZrO₂ ceramics at different sintering behaviors, and the relative density, Vickers hardness (H_v), and fracture toughness values were listed in Table 1 in detail. In Fig. 6 (a), the relative density grew first and then decreased at different sintering temperatures with the same holding time of 30 min and sintering rate of 0.2 $^{\circ}\text{C}/\text{min}$, and it was observed that the maximum value of $95.49 \pm 0.97\%$ took place at 1500 $^{\circ}\text{C}$. The organic in the ceramic bodies was removed through the previous debinding process, and the 3Y-ZrO₂ ceramics continued to undergo a solid-phase state in the subsequent sintering process. The rise of sintering temperature was accompanied with the increase of sintering energy and driving force, which led to powder densification. However, the relative density dropped to $94.29 \pm 0.37\%$ at 1550 $^{\circ}\text{C}$ where the migration rate of the pore was much lower than that of the grain boundary. Related to the relative density, the H_v and fracture toughness had the same trend that they increased first and then decreased. The maximum values of $12.11 \pm 0.23\text{ GPa}$ and $6.04 \pm 0.12\text{ MPa}\cdot\text{m}^{1/2}$ also occurred at 1500 $^{\circ}\text{C}$, respectively. In accordance, when the sintering temperature rose to 1550 $^{\circ}\text{C}$, the H_v and fracture toughness values decreased to $10.14 \pm 0.22\text{ GPa}$ and $5.24 \pm 0.11\text{ MPa}\cdot\text{m}^{1/2}$, respectively. In Fig. 6 (b), similar to different sintering temperatures, the relative density, H_v , and fracture toughness increased first and then fell at different holding time with the same sintering temperature of 1500 $^{\circ}\text{C}$ and sintering rate of 0.2 $^{\circ}\text{C}/\text{min}$. The maximum values were $96.18 \pm 0.83\%$, $12.45 \pm 0.12\text{ GPa}$, and $6.31 \pm 0.06\text{ MPa}\cdot\text{m}^{1/2}$ with 60 min,

respectively, for the reason that the grain grew and the pore migrated gradually with the improvement of holding time. When the holding time exceeded 60 min, the relative density declined to 94.37 ± 0.26 % due to the abnormal grain growth and uneven grain distribution, which also affected the H_v and fracture toughness of the sintered 3Y-ZrO₂ ceramics. In Fig. 6 (c), there was a similar trend in the mechanical properties at different sintering rates with the same sintering temperature of 1500 °C and holding time of 30 min. The maximum relative density, H_v , and fracture toughness were 95.87 ± 0.44 %, 13.30 ± 0.48 GPa, and 6.35 ± 0.23 MPa·m^{1/2} with 4 °C/min, respectively. The grain grew and the pore migrated steadily with a reasonable sintering rate, while the incomplete grain growth and pore migration would happen with a high sintering rate. As a result, the relative density, H_v and fracture toughness decreased to 95.31 ± 0.31 %, 12.27 ± 0.28 GPa and 5.60 ± 0.13 MPa·m^{1/2} with 8 °C/min, respectively. In summary, a sintering temperature of 1500 °C, a holding time of 60 min, and a sintering rate of 4 °C/min was one of the optimal sintering behaviors to obtain better mechanical properties of the sintered 3Y-ZrO₂ ceramics.

Inset Fig. 6 Here.

Inset Table 1 Here.

Fig. 7 presents the fracture microstructure and EDS of the printed and debinded 3Y-ZrO₂ ceramics. As presented in Fig. 7 (a), 3Y-ZrO₂ ceramic powders were dispersed with the various resins in the printed samples, and EDS analysis proved a large amount of C elements which was accounted for 44.26 wt.%. Fig. 7 (b) showed that a great quantity 3Y-ZrO₂ ceramic powders were agglomerated without no apparent resins. The C elements decreased to 2.59 wt.% indicated by EDS analysis, which demonstrated that the resins were almost exhausted in the debinding process.

Inset Fig. 7 Here.

Fig. 8 shows the fracture microstructure of the sintered 3Y-ZrO₂ ceramics at different sintering temperatures with the same holding time of 30 min and sintering rate of

0.2 °C/min. There were apparent intergranular fractures in the microstructure of the sintered 3Y-ZrO₂ ceramics. In Fig. 8 (a), the ceramic powders were densified to a solid-phase state at 1400 °C. However, there were a large amount of pores in the sintered samples, which lowered the relative density, H_v and fracture toughness. The grains grew and the grain boundary became smooth with the improvement of sintering temperature, accompanied with the increase in the mechanical properties of sintered samples. However, there existed some pores in the sample at 1550 °C (Fig. 8 b) compared with the microstructure of the sintered sample at 1500 °C (Fig. 8 c). Thus, the relative density, H_v and fracture toughness of the sintered samples were enhanced, while these mechanical properties of the sample at 1500 °C were larger than those of the sample at 1450 °C. As presented in Fig. 8 (d), the grain grew abnormally and the grain size became large, resulting to the worst mechanical properties of the sintered sample at 1550 °C. Meanwhile, there were some transgranular fractures in the microstructure of the sample at 1550 °C. Fig. 9 presents the fracture microstructure of the sintered 3Y-ZrO₂ ceramics at different holding time with the same sintering temperature of 1500 °C and sintering rate of 0.2 °C/min. There were no obvious pores in the microstructure of the sintered samples. In Fig. 9 (a), there was insufficient time for the grain to grow without holding time, and the grain size was too small to reduce the mechanical properties of the sintered sample. As shown in Fig. 9 (b,c), the grain continued to grow and the grain size became large at 30 min and 60 min. As a result, the relative density, H_v and fracture toughness of these samples improved. However, when the holding time exceeded 60 min, there were some abnormal grain growth and transgranular fractures in the microstructure, leading to the mechanical properties of the sintered sample at 90 min. Fig. 10 displays the fracture microstructure of the sintered 3Y-ZrO₂ ceramics at different sintering rates with the same sintering temperature of 1500 °C and holding time of 30 min. As presented in Fig. 10 (a-c), there were no apparent difference in the microstructure of the sintered samples at 2 °C/min, 4 °C/min, and 6 °C/min. In accordance, the relative density, H_v and fracture toughness of these samples presented no obvious discrepancy with a reasonable sintering rate. In Fig. 10 (d), there existed the incomplete grain growth and transgranular fractures in the microstructure at 8 °C/min.

Thus, the worst mechanical properties of the sintered samples took place due to the high sintering rate.

Inset Fig. 8 Here.

Inset Fig. 9 Here.

Inset Fig. 10 Here.

Fig. 11 shows the X-ray diffraction (XRD) patterns of the printed, debinded, and sintered samples at different sintering behaviors. The printed sample consisted of both monoclinic phase and tetragonal phase at room temperature. There was a similar XRD spectra in the debinded sample at 1000 °C. However, all the monoclinic phase transformed into the tetragonal phase for all sintered samples at different sintering behaviors. The Y^{3+} ions had a certain degree of stability in ZrO_2 , which hindered the transformation of t to m and thus reduced the temperature of $t \rightarrow m$ phase transition of ZrO_2 ceramics [36]. Meanwhile, the XRD analysis indicated that there was no change in crystal transformation and phase composition of the sintered 3Y- ZrO_2 ceramics at different sintering conditions.

Inset Fig. 11 Here.

4. Conclusions and future work

3Y- ZrO_2 ceramics at different sintering behaviors in air atmosphere were obtained in this study. Firstly, the curing properties of homemade 3Y- ZrO_2 pastes were studied for the fabrication of the green parts. Then, the dimensional accuracy, surface quality, and mechanical properties of the sintered samples were thoroughly investigated. The main conclusions are as follows:

(1) Cure depth and cure width of the 3Y- ZrO_2 suspensions increased with the increase of laser power while the decrease of scanning speed. Referring to the Beer-Lambert law, the penetration depth and critical exposure values of the suspensions were calculated as 17.2 μm and 4.80 mJ/cm^2 , respectively. Despite of different sintering behaviors, the

shrinkage ratios were 26%~27 %, 30%~31 %, and 27%~33 % in the length, width, and height direction, respectively.

(2) The surfaces of SLA-printed 3Y-ZrO₂ ceramics presented a clearly anisotropic feature, and there was an obvious layer-and-layer process in the YOZ and XOZ surfaces. Compared with the printed samples, an increase of Ra value took place in the sintered samples at different sintering behaviors. The Ra values of XOY, YOZ, and XOZ surfaces were smallest as 0.52 μm, 2.40 μm, and 2.46 μm at 1500 °C with a holding time of 30 min and sintering rate of 0.2 °C/min, respectively.

(3) The relative density, Vickers hardness (H_v), and fracture toughness values showed a similar trend at different sintering behaviors, which increased first and then fell. There were a large amount pores in the microstructures at a low temperature, while the abnormal growth and uneven distribution occurred at a high temperature, holding time, and sintering rate. The phenomenon demonstrated a poor mechanical properties of the sintered samples, accompanied with some transgranular fractures in the microstructure. The optimal parameters were 1500 °C, 60 min, and 4 °C/min, and the maximum relative density of 96.18 %, Vickers hardness of 12.45 GPa, and fracture toughness of 6.35 MPa·m^{1/2} were achieved.

(4) Indicated by EDS analysis, the comparison between the printed and debinded samples revealed the resin was rarely remained in the debinding process. Furthermore, XRD analysis showed that all the monoclinic phase transformed into the tetragonal phase, indicating that there was no change in crystal transformation and phase composition of the sintered 3Y-ZrO₂ ceramics at different sintering conditions.

The main focus of this study is to explore the dimensional accuracy, surface quality, and mechanical properties of SLA-printed 3Y-ZrO₂ ceramics at different sintering behaviors, and thus the optimal parameters are proposed to provide a practical guiding significance for fabricating 3Y-ZrO₂ ceramics in the biological applications. In future work, the biocompatibility and cell culture experiments of sintered 3Y-ZrO₂ ceramics shall be investigated.

Acknowledgements

This project was supported by the Shandong Provincial Natural Science Foundation, China (Grant No.ZR2017MEE052; No.ZR2018ZB0105), the Shandong Provincial Key Research and Development Program (Grant No.2019JZZY010441). Thanks for all the former researches contributed to this study.

References

- [1] Lian Q, Sui WQ, Wu XQ, *et al.* Additive manufacturing of ZrO₂ ceramic dental bridges by stereolithography. *Rapid Prototyping J* 2018, **24**: 114-119.
- [2] Matei M, Voinea EA, Rica R, *et al.* New zirconia-based materials for dental applications. Structural, morphological and histological evaluation. *Ceram Int* 2019, **45**: 14859-14866.
- [3] Fu L, Engqvist H, Xia W. Highly translucent and strong ZrO₂-SiO₂ nanocrystalline glass ceramic prepared by sol-gel method and spark plasma sintering with fine 3D microstructure for dental restoration. *J Eur Ceram Soc* 2017, **37**: 4067-4081.
- [4] Zhang C, Wang FL, Jiang ZL, *et al.* Effect of graphene oxide on the mechanical, tribological, and biological properties of sintered 3Y-ZrO₂/GO composite ceramics for dental implants. *Ceram Int* 2021, **47**: 6940-6946.
- [5] Cooper LF, Stanford C, Feine J, *et al.* Prospective assessment of CAD/CAM zirconia abutment and lithium disilicate crown restorations: 2.4 year results. *J Prosthet Dent* 2016, **116**: 33-39.
- [6] Alao AR, Stoll R, Song XF, *et al.* Surface quality of yttria-stabilized tetragonal zirconia polycrystal in CAD/CAM milling, sintering, polishing and sandblasting processes. *J Mech Behav Biomed* 2017, **65**: 102-116.
- [7] Nair A, Prithviraj DR, Regish KM, *et al.* Custom milled zirconia implant supporting a ceramic zirconia restoration: a clinical report. *Kathmandu Univ Med J* 2013, **44**: 328-331.
- [8] Chen Z, Sun XH, Shang YP, *et al.* Dense ceramics with complex shape fabricated by 3D printing: A review. *J Adv Ceram* 2021, **10**: 195-218.
- [9] Rasaki SA, Xiong DY, Xiong SF, *et al.* Photopolymerization-based additive manufacturing of ceramics: A systematic review. *J Adv Ceram* 2021, **10**: 442-471.
- [10] Revilla-Leon M, Methani MM, Morton D, *et al.* Internal and marginal discrepancies associated with stereolithography (SLA) additively manufactured zirconia crowns. *J Prosthet Dent* 2020, **124**:

730-737.

[11] Fan YH, Feng B, Yang LL, *et al.* Application of artificial neural network optimization for resilient ceramic parts fabricated by direct ink writing. *Int J Appl Ceram Tec* 2020, **17**: 217-226.

[12] Gao SY, Wang C, Xing BH, *et al.* Experimental investigation on bending behavior of ZrO₂ honeycomb sandwich structures prepared by DLP stereolithography. *Thin Wall Struct* 2020, **157**: 107099.

[13] Abdullah AM, Rahim TNAT, Hamad WNF, *et al.* Mechanical and cytotoxicity properties of hybrid ceramics filled polyamide 12 filament feedstock for craniofacial bone reconstruction via fused deposition modelling. *Dent Mater* 2018, **34**: E309-E316.

[14] Ferrage L, Bertrand G, Lenormand P. Dense yttria-stabilized zirconia obtained by direct selective laser sintering. *Addit Manuf* 2018, **21**: 472-478.

[15] Guan JR, Wang QP, Zhang XW, *et al.* Selective laser melting of yttria-stabilized zirconia. *Mater Res Express* 2019, **6**: 015402.

[16] Chinelatto ASA, Chinelatto AL, Ojaimi CL, *et al.* Effect of sintering curves on the microstructure of alumina-zirconia nanocomposites. *Ceram Int* 2014, **40**: 14669-14676.

[17] Fan J, Lin T, Hu F, *et al.* Effect of sintering temperature on microstructure and mechanical properties of zirconia toughened alumina machinable dental ceramics. *Ceram Int* 2017, **43**: 3648-3653.

[18] Li H, Liu YS, Liu YS, *et al.* Effect of sintering temperature in argon atmosphere on microstructure and properties of 3D printed alumina ceramic cores. *J Adv Ceram* 2020, **9**: 220-231.

[19] Xing HY, Zou B, Li SS, *et al.* Study on surface quality, precision and mechanical properties of 3D printed ZrO₂ ceramic components by laser scanning stereolithography. *Ceram Int* 2017, **43**: 16340-16347.

[20] Wu HD, Liu W, Lin LF, *et al.* Preparation of alumina-toughened zirconia via 3D printing and liquid precursor infiltration: manipulation of the microstructure, the mechanical properties and the low temperature aging behavior. *J Mater Sci* 2019, **54**: 7447-7459.

[21] Zheng TQ, Wang W, Sun JX, *et al.* Development and evaluation of Al₂O₃-ZrO₂ composite processed by digital light 3D printing. *Ceram Int* 2020, **46**: 8682-8688.

[22] Liu XY, Zou B, Xing HY, *et al.* The preparation of ZrO₂-Al₂O₃ composite ceramic by SLA-3D printing and sintering processing. *Ceram Int* 2020, **46**: 937-944.

- [23] Zhang C, Jiang ZL, Zhao L, *et al.* Stability, rheological behaviors, and curing properties of 3Y–ZrO₂ and 3Y–ZrO₂/GO ceramic suspensions in stereolithography applied for dental implants. *Ceram Int* 2021, **47**: 13344-13350.
- [24] Singh G, Missiaen JM, Bouvard D, *et al.* Copper additive manufacturing using MIM feedstock: adjustment of printing, debinding, and sintering parameters for processing dense and defectless parts. *Int J Adv Manuf Tech* 2021, DOI: [10.1007/s00170-021-07188-y](https://doi.org/10.1007/s00170-021-07188-y).
- [25] Gu JH, Qiao L, Cai W, *et al.* Effects of heating rate in thermal debinding on the microstructure and property of sintered NiCuZn ferrite prepared by powder injection molding. *J Magn Magn Mater* 2021, **530**: 167931.
- [26] Chen QH, Zou B, Lai QG, *et al.* A study on biosafety of HAP ceramic prepared by SLA-3D printing technology directly. *J Mech Behav Biomed* 2019, **98**: 327-335.
- [27] Gentry SP, Halloran JW. Light scattering in absorbing ceramic suspensions: effect on the width and depth of photopolymerized features. *J Eur Ceram Soc* 2015, **35**: 1895-1904.
- [28] Rueggeberg FA, Caughman WF, Jr CJ. Effect of light intensity and exposure duration on cure of resin composite. *Operat Dent* 1994, **19**: 26-32.
- [29] Lu JH, Youngblood JP. Adhesive bonding of carbon fiber reinforced composite using UV-curing epoxy resin. *Compos B Eng* 2015, **82**: 221-225.
- [30] Feng CW, Zhang KQ, He RJ, *et al.* Additive manufacturing of hydroxyapatite bioceramic scaffolds: Dispersion, digital light processing, sintering, mechanical properties, and biocompatibility. *J Adv Ceram* 2020, **9**: 360-373.
- [31] Yao YX, Qin W, Xing BH, *et al.* High performance hydroxyapatite ceramics and a triply periodic minimum surface structure fabricated by digital light processing 3D printing. *J Adv Ceram* 2021, **1**: 39-48.
- [32] Cho S, Jeong D, Kim H. Influence of powder characteristics on shrinkage behavior of 3D-printed glass structures. *Ceram Int* 2020, **46**: 16827-16832.
- [33] Xing HY. Study on preparation method and forming properties of ceramic paste with high solid content for stereolithography 3D printing. *A Dissertation for Doctoral Degree, Shandong University*. 2020, 83 (In Chinese).
- [34] Li F, Huang X, Liu JX, *et al.* Sol-gel derived porous ultra-high temperature ceramics. *J Adv Ceram* 2020, **9**: 1-16.

[35] Hassanin H, Essa K, Elshaer A, *et al.* Micro-fabrication of ceramics: Additive manufacturing and conventional technologies. *J Adv Ceram* 2021, **10**: 1-27.

[36] Pereira GKR, Venturini AB, Silvestri T, *et al.* Low-temperature degradation of Y-TZP ceramics: A systematic review and meta-analysis. *J Mech Behav Biomed* 2016, **55**: 151-163.

Figures

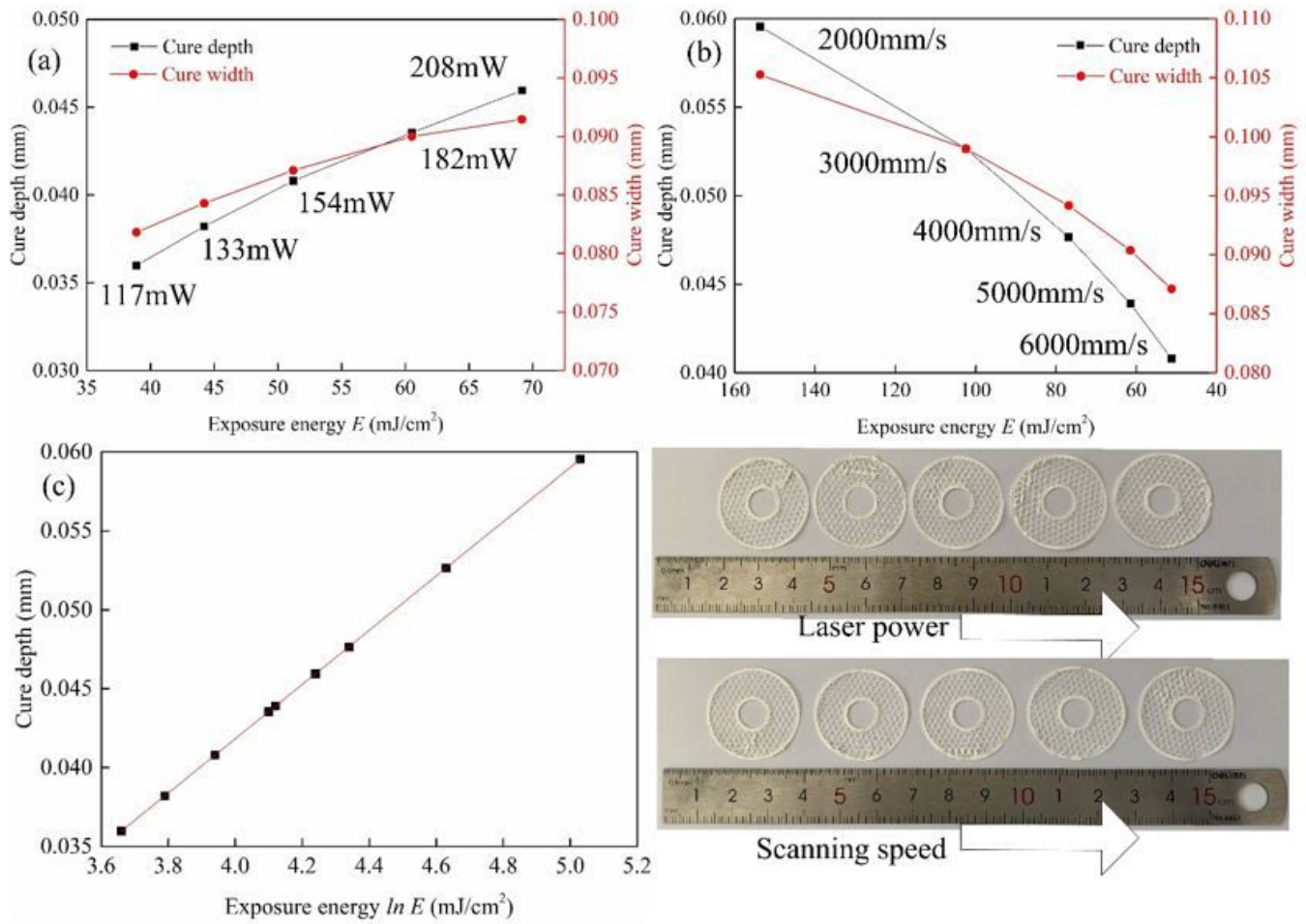


Figure 1

Cure depth and cure width of the 3Y-ZrO₂ suspensions (a) at different laser powers with the same scanning speed of 6000 mm/s; (b) at different scanning speeds with the same laser power of 154 mW; (c) Linear fit of cure depth C_d and exposure energy $\ln E$.

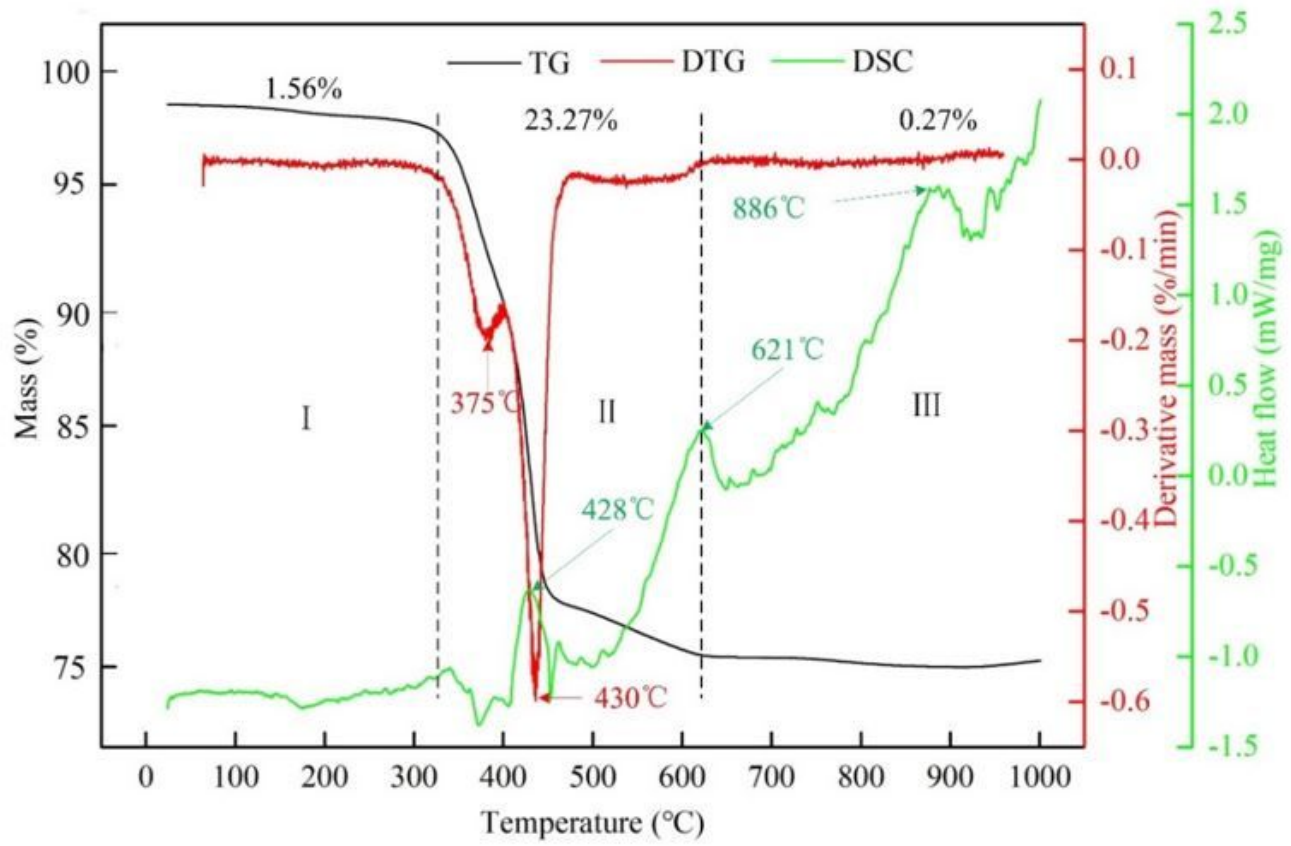


Figure 2

TG-DTG and DSC curves for thermogravimetric and differential scanning calorimetry of the SLA-printed 3Y-ZrO₂ green bodies.

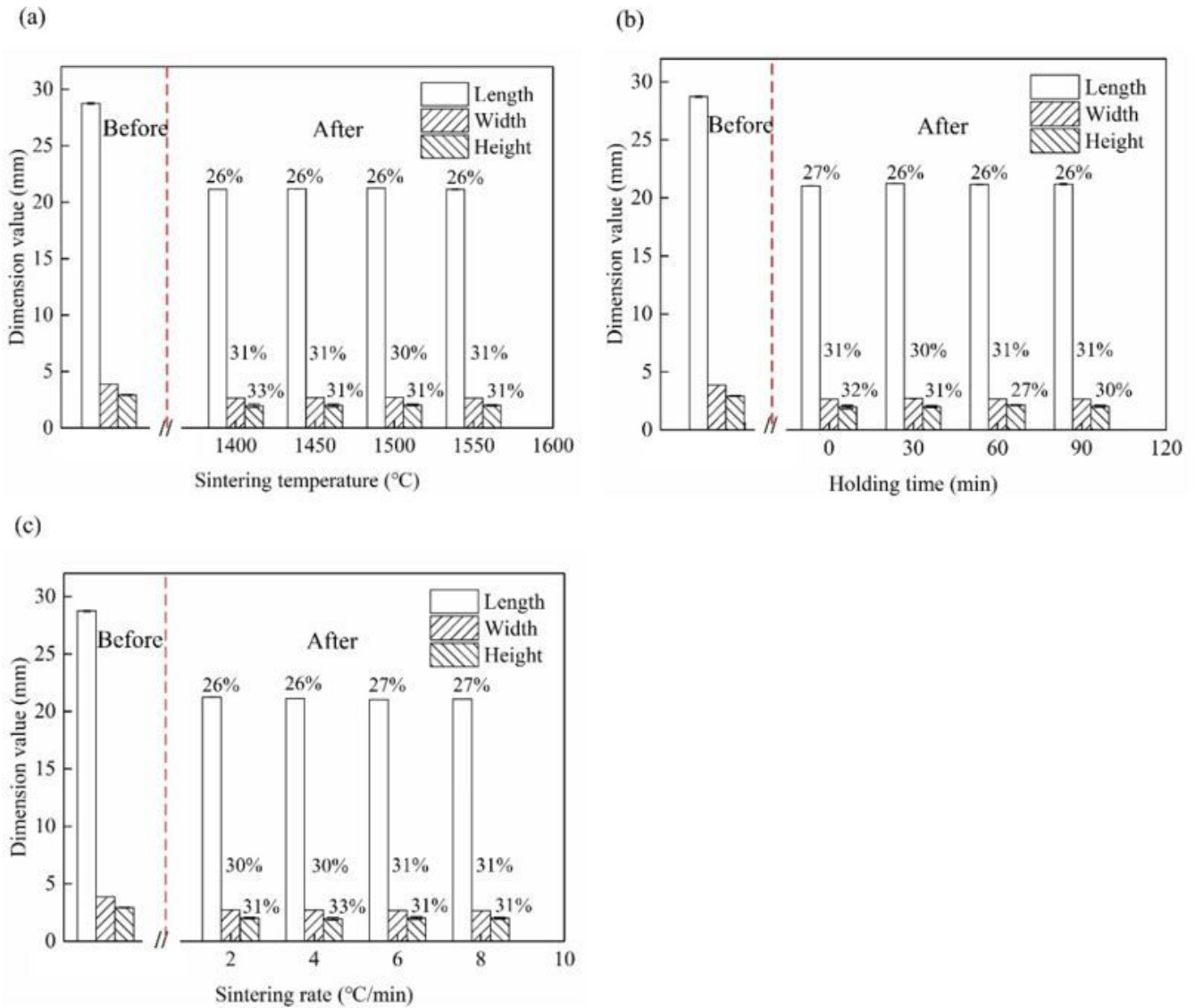


Figure 3

Length, width, and height of the sintered 3Y-ZrO₂ ceramics (a) at different sintering temperatures with the same holding time of 30 min and sintering rate of 0.2 °C/min; (b) at different holding time with the same sintering temperature of 1500 °C and sintering rate of 0.2 °C/min; (c) at different sintering rates with the same sintering temperature of 1500 °C and holding time of 30 min.

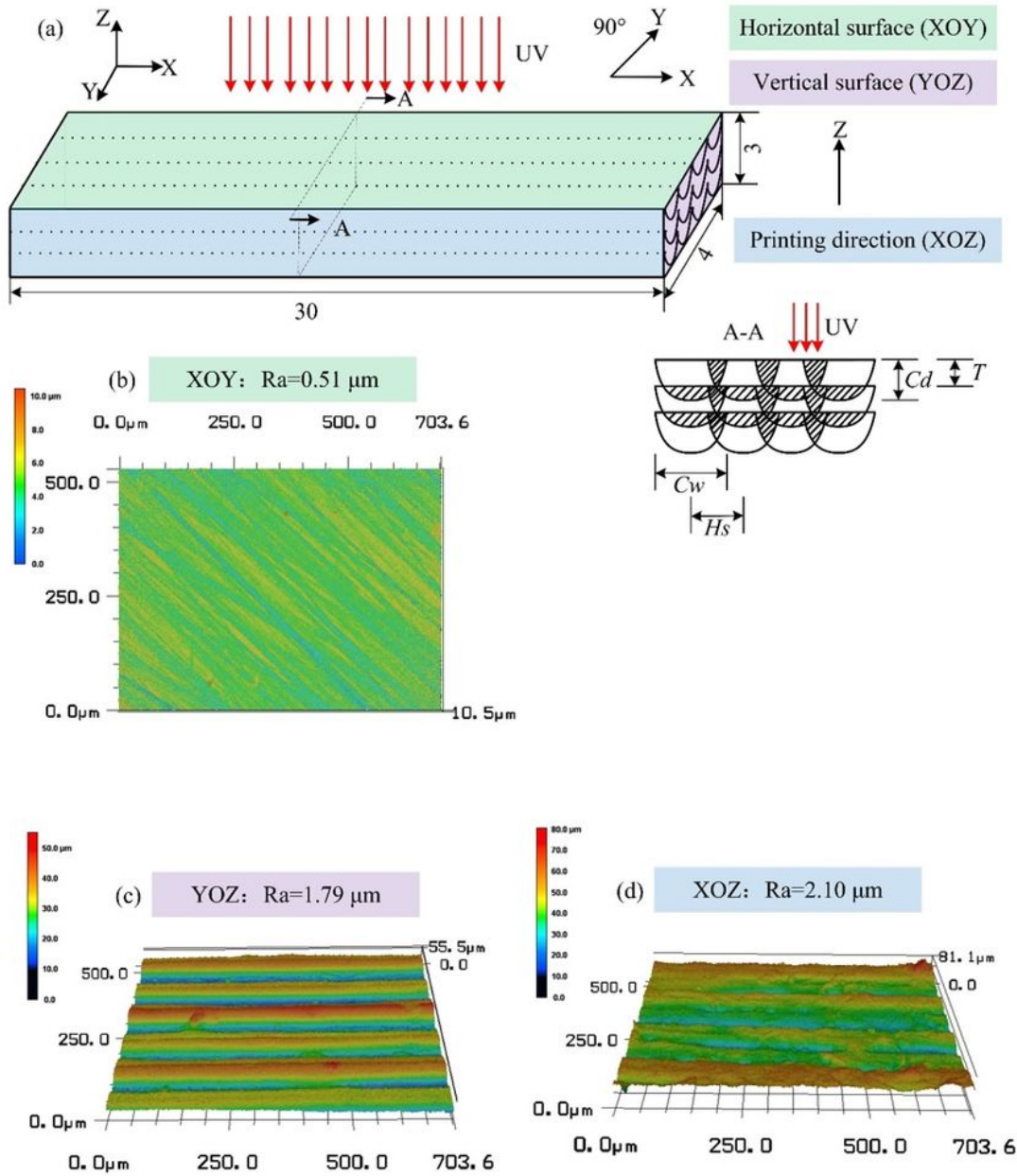


Figure 4

(a) Schematic of the fabrication process of 3Y-ZrO₂ ceramics by SLA; (b-d) 3D morphology and surface roughness of XOY, YOZ, and XOZ surfaces of green bodies, respectively.

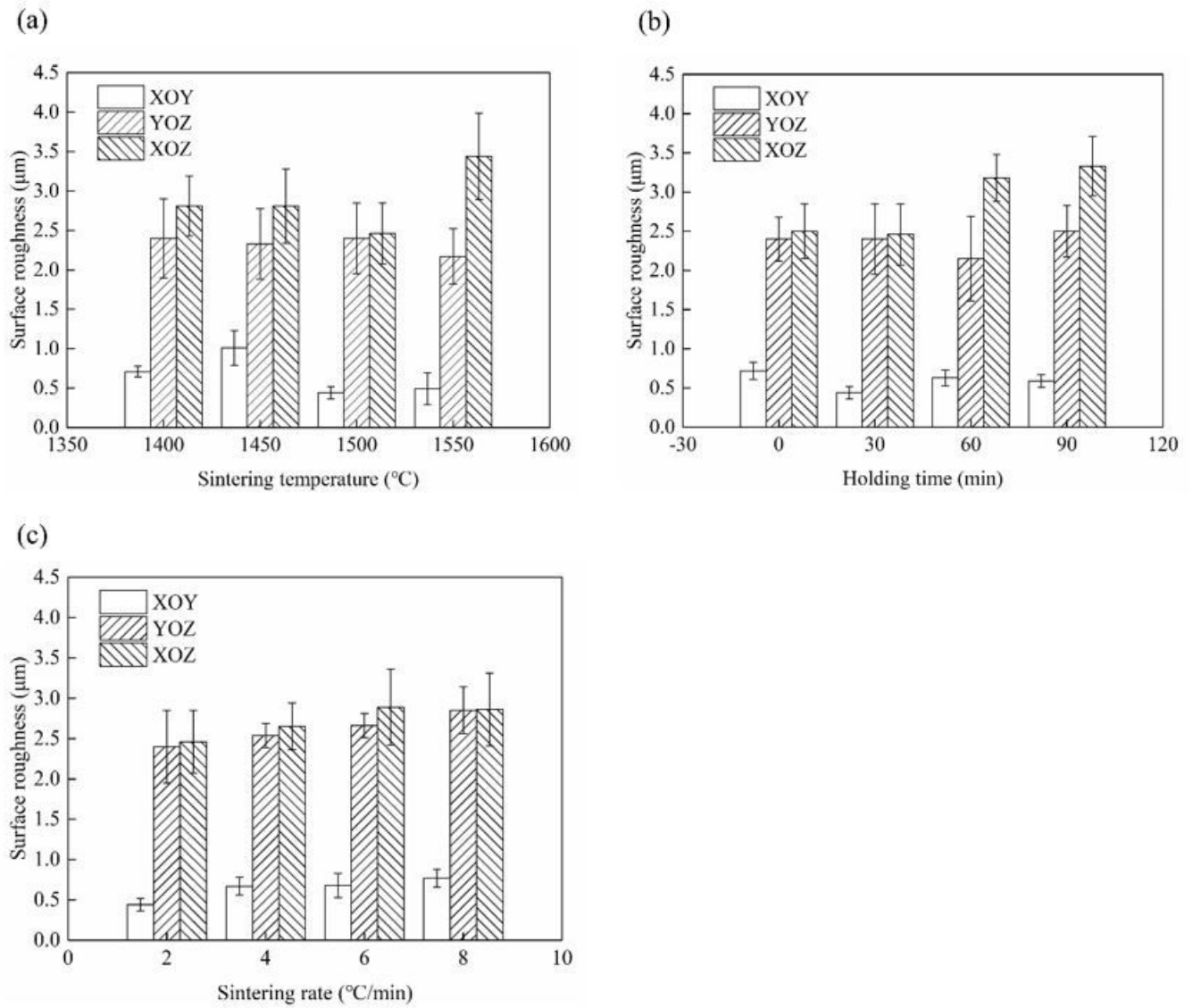


Figure 5

Surface roughness of XOY, YOZ, and XOZ surfaces of the sintered 3Y-ZrO₂ ceramics (a) at different sintering temperatures with the same holding time of 30 min and sintering rate of 0.2 $^{\circ}\text{C}/\text{min}$; (b) at different holding time with the same sintering temperature of 1500 $^{\circ}\text{C}$ and sintering rate of 0.2 $^{\circ}\text{C}/\text{min}$; (c) at different sintering rates with the same sintering temperature of 1500 $^{\circ}\text{C}$ and holding time of 30 min.

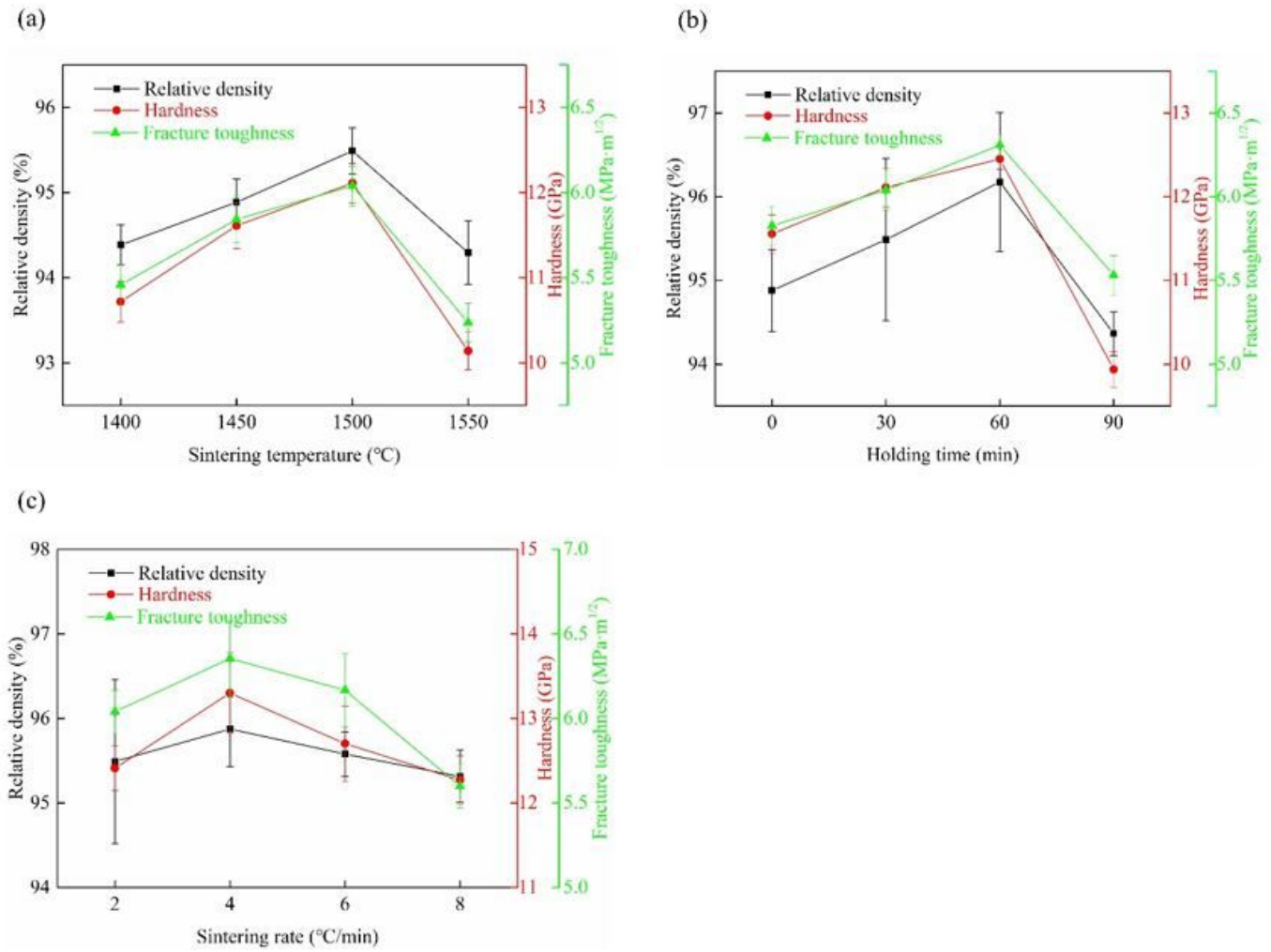


Figure 6

Mechanical properties of the sintered 3Y-ZrO₂ ceramics (a) at different sintering temperatures with the same holding time of 30 min and sintering rate of 0.2 °C/min; (b) at different holding time with the same sintering temperature of 1500 °C and sintering rate of 0.2 °C/min; (c) at different sintering rates with the same sintering temperature of 1500 °C and holding time of 30 min.

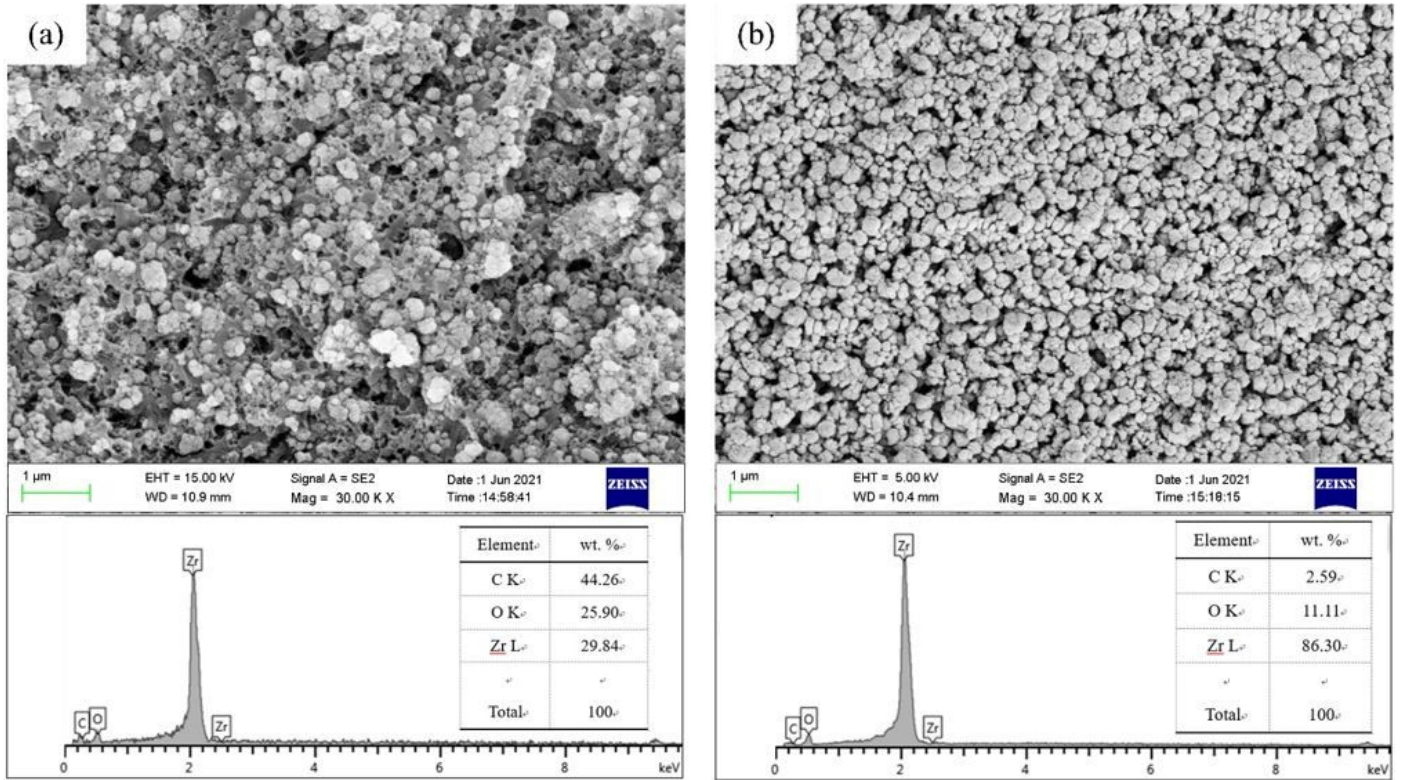


Figure 7

Fracture microstructure and EDS of (a) the printed 3Y-ZrO₂ ceramics; (b) the debinded 3Y-ZrO₂ ceramics.

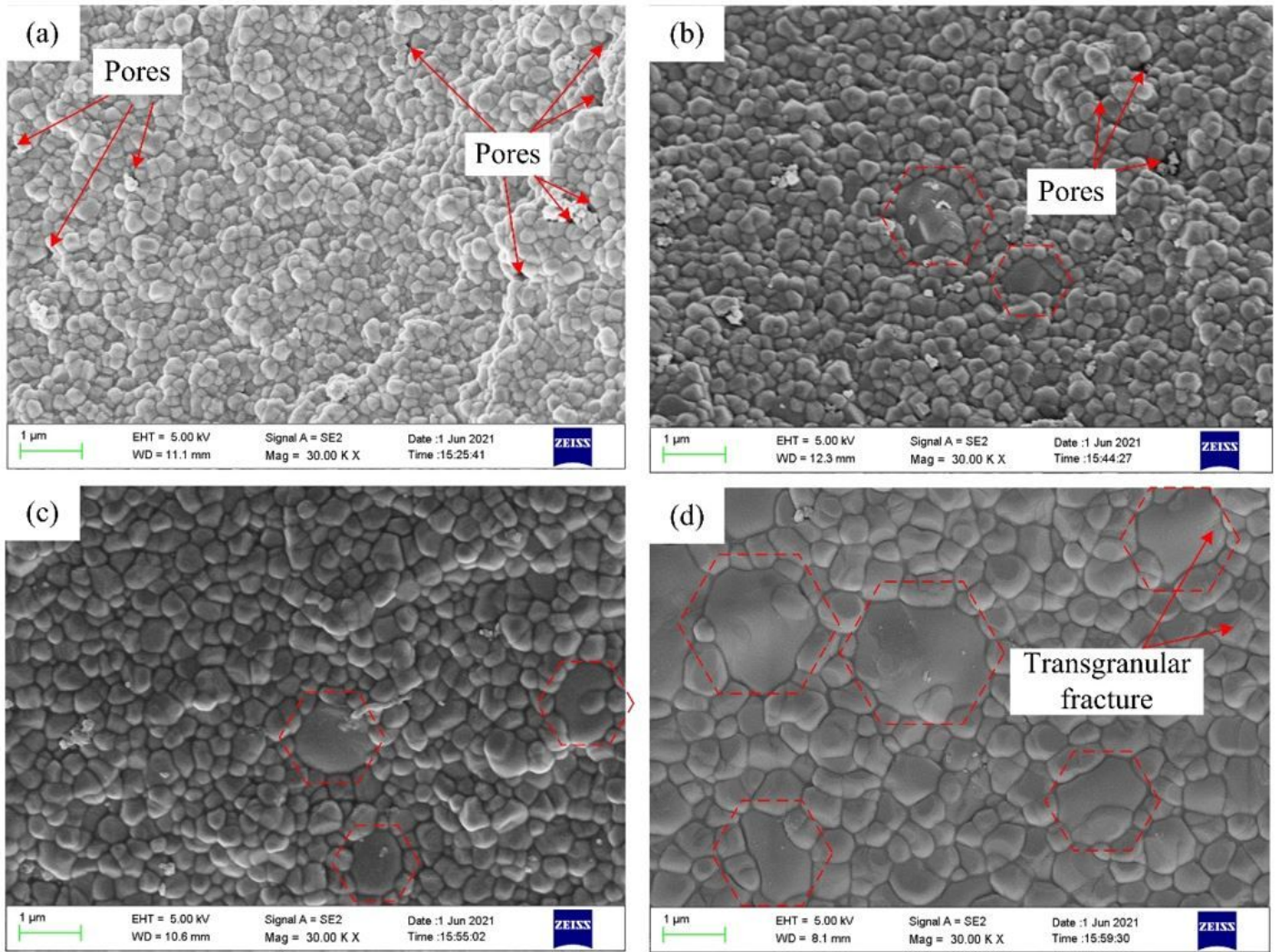


Figure 8

Fracture microstructure of the sintered 3Y-ZrO₂ ceramics (a) 1400 °C; (b) 1450 °C; (c) 1500 °C; (d) 1550 °C with the same holding time of 30 min and sintering rate of 0.2 °C/min.

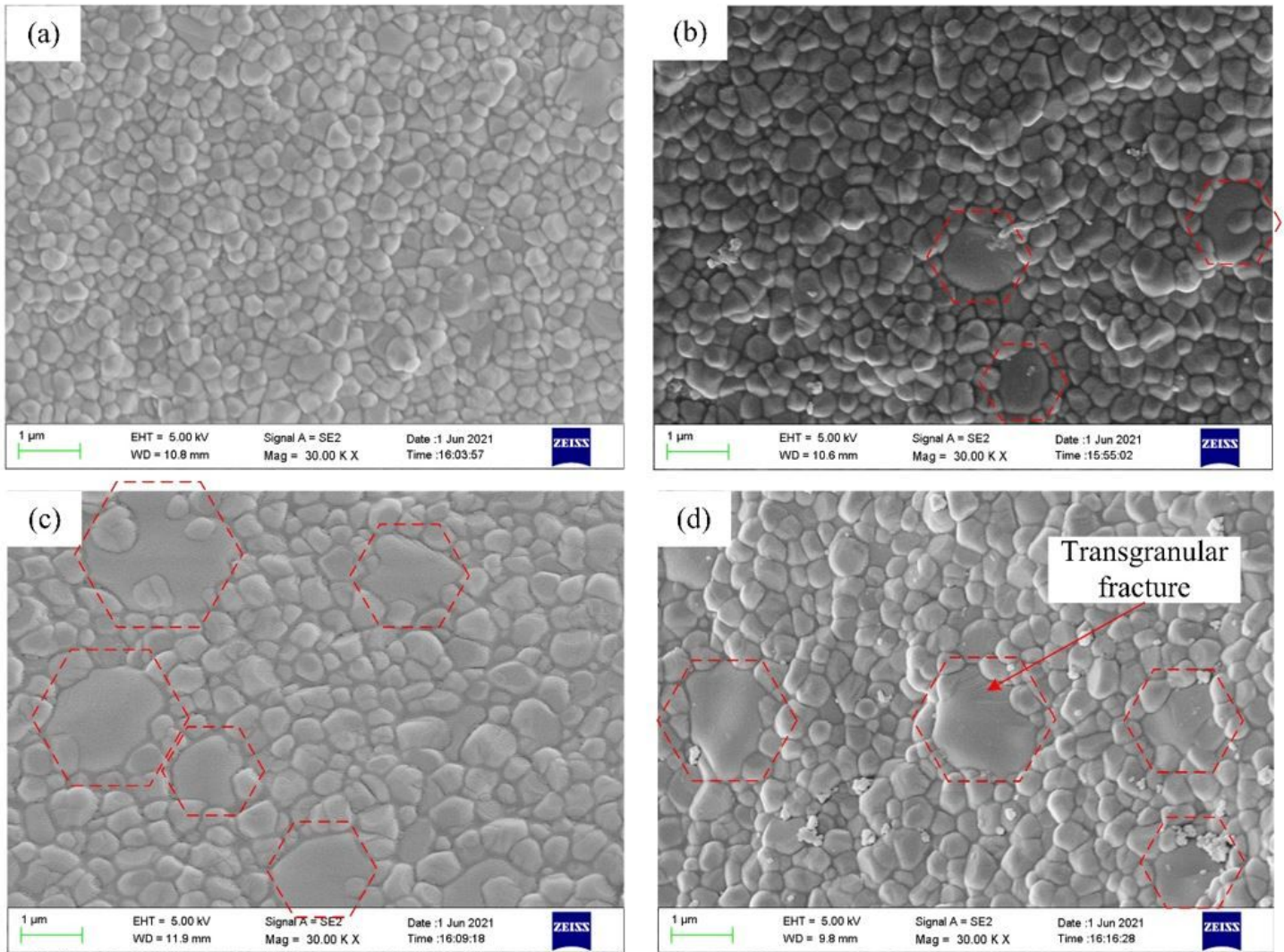


Figure 9

Fracture microstructure of the sintered 3Y-ZrO₂ ceramics (a) 0 min; (b) 30 min; (c) 60 min; (d) 90 min with the same sintering temperature of 1500 °C and sintering rate of 0.2 °C/min.

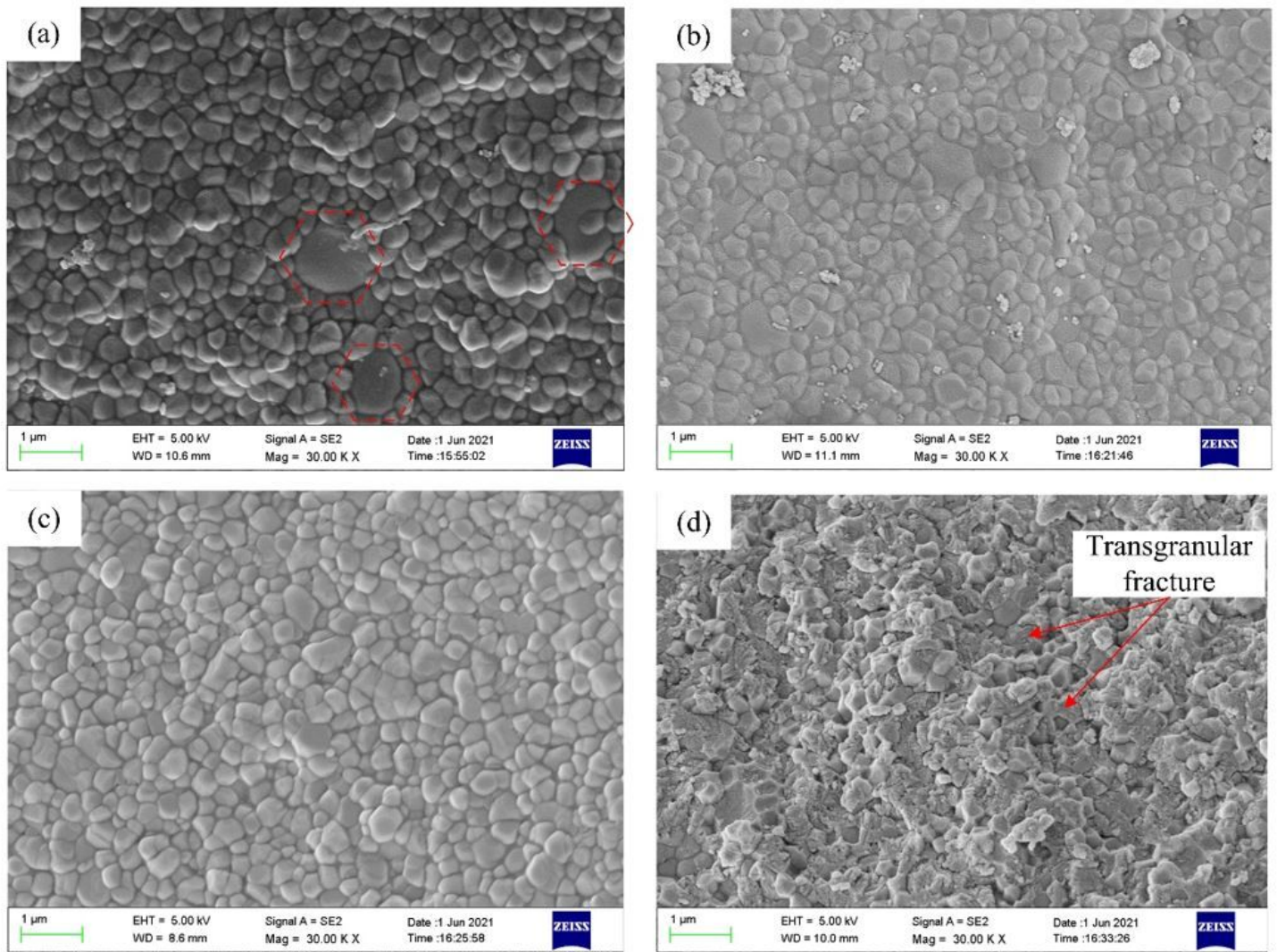


Figure 10

Fracture microstructure of the sintered 3Y-ZrO₂ ceramics (a) 2 °C/min; (b) 4 °C/min; (c) 6 °C/min; (d) 8 °C/min with the same sintering temperature of 1500 °C and holding time of 30 min.

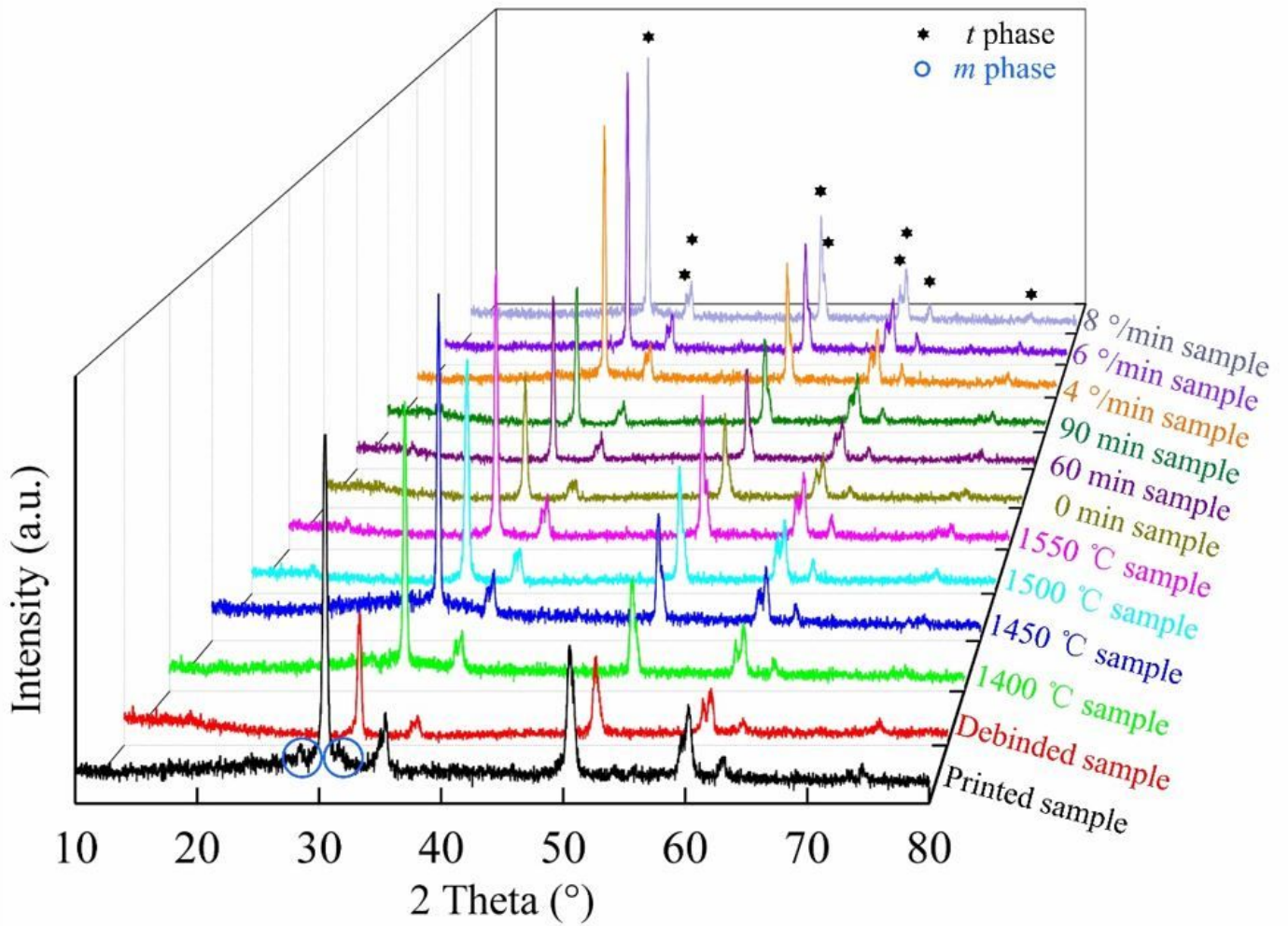


Figure 11

X-ray diffraction (XRD) patterns of the printed, debinded, and sintered samples at different sintering behaviors.